

Article

Zircon and Garnet U–Pb Ages of the Longwan Skarn Pb–Zn Deposit in Guangxi Province, China and Their Geological Significance

Xuejiao Zhang ^{1,2}, Wei Ding ^{1,2,*}, Liyan Ma ^{1,2}, Wei Fu ^{1,2,3} , Xijun Liu ^{1,2} and Saisai Li ^{1,2}¹ College of Earth Sciences, Guilin University of Technology, Guilin 541004, China² Guangxi Key Laboratory of Hidden Metallic Ore Deposits Exploration, Guilin University of Technology, Guilin 541004, China³ Collaborative Innovation Center for Exploration of Nonferrous Metal Deposits and Efficient Utilization of Resources by the Province and Ministry, Guilin University of Technology, Guilin 541004, China

* Correspondence: dingwei@glut.edu.cn

Abstract: Garnet is the most common alteration mineral in skarn-type deposits, and the geochronological research on it can limit the mineralization age. The Longwan Pb–Zn deposit, situated within the Fozichong Pb–Zn ore field in Guangxi, lacks precise geochronological data, limiting the in-depth comprehension of its genesis and tectonic setting. This study employs LA-ICP-MS U–Pb dating of garnets developed in the skarn orebody and zircons in the associated granitic porphyry to determine the deposit’s mineralization age. Backscatter electron images and electron probe microanalysis reveal common zonation characteristics in garnets from the Longwan Pb–Zn deposit, with dominant end-member compositions of Andradite and Grossular. The values of U concentrations range from 1.8 ppm to 3.7 ppm, and a garnet U–Pb age of 102.6 ± 1.9 Ma was obtained, consistent with the zircon U–Pb age of 102.1 ± 1.2 Ma from the granite porphyry within the deposit. The Longwan Pb–Zn deposit formed during the late Early Cretaceous as a skarn deposit resulting from contact metasomatism between the granite porphyry and the host rock. The deposit likely formed in response to the Neo-Tethys plate subducting beneath the South China continent during the Cretaceous, followed by a retreat during the Late Cretaceous. The Cenxi-Bobai Fault experienced reactivation under the extensional tectonic regime induced by the Neo-Tethys Ocean’s retreat, leading to a series of magmatic activities along the NE-trending direction within the Fault. The Longwan Pb–Zn deposit formed during the processes of magma emplacement and contact metasomatic reactions with the country rock.

Keywords: garnet; granite porphyry; ore-forming age; tectonic setting

Citation: Zhang, X.; Ding, W.; Ma, L.; Fu, W.; Liu, X.; Li, S. Zircon and Garnet U–Pb Ages of the Longwan Skarn Pb–Zn Deposit in Guangxi Province, China and Their Geological Significance. *Minerals* **2023**, *13*, 644. <https://doi.org/10.3390/min13050644>

Academic Editor: Maria Boni

Received: 24 March 2023

Revised: 25 April 2023

Accepted: 2 May 2023

Published: 6 May 2023



Copyright: © 2023 by the authors. Licensee MDPI, Basel, Switzerland. This article is an open access article distributed under the terms and conditions of the Creative Commons Attribution (CC BY) license (<https://creativecommons.org/licenses/by/4.0/>).

1. Introduction

Geochronological investigations play a pivotal role in deciphering the genesis and mineralization processes of ore deposits. With the advancements in analytical techniques, various dating methods have been extensively applied in metallic ore deposit studies, such as ⁴⁰Ar–³⁹Ar, U–Pb, Sm–Nd, Rb–Sr, and Re–Os methods [1]. Garnet, a typical alteration mineral in the skarn deposits, has been widely utilized for tracing the geochemical evolution of hydrothermal fluids [2–4]. Recent research highlights the higher U–Pb closure temperature system (>850 °C) in garnets compared to other minerals [5], and the elevated levels of U and Pb in Andradite, fulfilling the LA-ICP-MS elemental testing requirements [6]. Consequently, garnets have garnered significant attention as subjects for geochronological research in the skarn deposits [1,7–11].

The Longwan lead–zinc mine, a large-scale deposit within the Fozichong lead–zinc ore field in the southeastern Pb–Zn–Ag–Au polymetallic metallogenic belt, has a cumulative proven metal content of 357,000 tons of lead and 546,000 tons of zinc with average grades

of 2.39% Pb and 3.66% Zn. Previous investigations on the Fozichong ore field, including the Longwan Pb–Zn deposit, sought to constrain the mineralization age through dating intrusive bodies [12]. However, due to the spatial relationship between the intrusive body and the ore body, especially when multiple magmatic events occur in the mining area, it is difficult to accurately determine the genetic relationship between the intrusive body and the skarn [13]. As a result, a direct ore-forming age for the Longwan Pb–Zn deposit has not been obtained, which hinders the understanding of the deposit's formation mechanism and its related tectonic and geodynamic background. Furthermore, the Longwan lead–zinc deposit lies at the transition zone between the South China-Pacific tectonic domain and the Tethyan tectonic domain. Its mineralization dynamics have been attributed to the westward subduction of the Pacific plate [14]; however other scholars propose that contemporaneous plutons near the Longwan deposit formed due to the northward subduction of the Neo-Tethys [15]. Abundant garnets are present in the skarn orebodies of the Longwan lead–zinc deposit. This study, based on the comprehensive geological features of the deposit, aims to determine the mineralization age by dating garnets in the Longwan skarn deposit and zircons in the associated granitic porphyry, providing robust evidence for deposit petrogenesis research. Integrating the mineralization age with previous tectonic evolution studies, this paper delves deeper into the mineralization dynamics background of the Longwan Pb–Zn deposit.

2. Geological Background

2.1. Regional Geological Features

The Longwan lead–zinc deposit is situated in southeastern Guangxi Province, China, and lies on the Cenxi-Bobai Fault zone in the southwest section of the Qin-Hang suture zone [16]. The deposit is situated at the junction of the South China Pacific tectonic domain and the Tethys tectonic domain. Cretaceous magmatic rocks are extensively distributed throughout the region (Figure 1a). The northeast-trending Cenxi-Bobai Fault zone represents a significant geological structure in southeastern Guangxi (Figure 1b). This deep fault zone is likely to have originated during the Sinian period (a geological time period, that spans from 850 Ma to 542 Ma) and has played a crucial role in controlling the distribution of rocks and ores, displaying multiple stages of activity that have induced various magmatic and tectonic events [14,17]. The late Yanshanian intrusive rocks in the region predominantly occur along the Cenxi-Bobai Fault zone, with granites being the primary rock type. They appear in the form of small plutons, and dykes (Figure 1c). The geological evolution of this area has experienced multiple tectonic events, including the Caledonian orogeny, the Hercynian-Indosinian collision orogeny, and the Yanshanian-Himalayan intraplate extension [18]. These tectonic events, coupled with intense magmatic activity, regional metamorphism, and migmatization, have formed the current complex geological structure [19] and led to multi-stage mineralization events [20,21]. Intermediate-acid magmatic rocks and volcanic rocks of the Yanshan period are primarily distributed along the NE–SW trending Cenxi-Bobai Fault zone, constituting a multiphase magmatic belt.

The geology of this region, with the exception of the Permian and Triassic systems, displays exposures spanning from the Cambrian to Cretaceous periods. Among these strata, the Lower Silurian and the Upper Ordovician are the most significant ore-bearing units in the Fozichong mining district [16]. The Ordovician strata primarily consist of sandstone, limestone, and siltstone, with slate being less common, and are predominantly distributed in the central and eastern parts of the mining area. The Silurian strata are characterized by dark gray slate interbedded with sandstone, siltstone, mudstone with limestone, and fine-grained sandstone, mainly found in the western part of the mining area. The Devonian strata have isolated remnants in the southwestern portion of the study area, featuring the lower section with sandstone interbedded with thin layers of limestone and the upper section composed of marble [19]. The mining area showcases an abundance of folds and fault structures, with the NE–NNE trending thrust-fold belt serving as the primary structural framework [14,22]. Intense magmatic activity within the Fozichong ore

field is marked by a diverse range of lithologies and complex lithofacies characteristics. The late Hercynian and Yanshanian (a geological event that occurred during the Mesozoic era, mainly affecting eastern China) intrusive acidic and intermediate-acid magmatic rocks, such as biotite monzonitic granite and granodiorite, are dominant [14,23–26]. These rocks provide ideal subjects for studying and refining the genetic mechanisms and tectonic background of Late Mesozoic magmatic activity in South China.

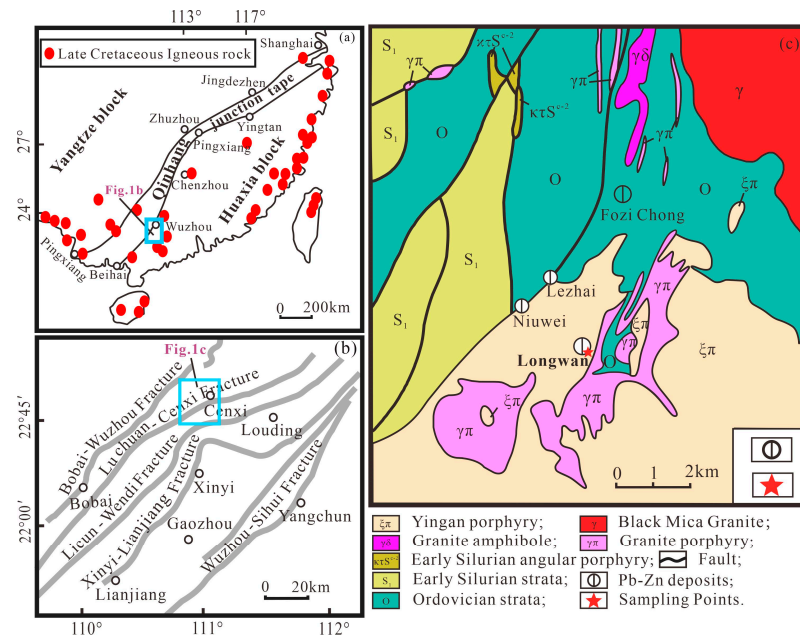


Figure 1. Geotectonic position (a) and regional structural domain map (b,c) of the Fozichong geological map from field mapping. (a) Modified after [27]; (b) modified after [27]; and (c) modified after [12].

2.2. Geological Characteristics of the Ore Deposit

The Longwan Pb–Zn deposit is situated within the Fozichong ore field, which hosts numerous Pb–Zn deposits, including the Fozichong, Niuwei, Longwan and Lezhai Pb–Zn deposits, and other mining sites.

The deposit is located at the southern margin of the Fozichong mining district and the southeastern block of the Niwei Fault. The Longwan mining area is relatively small, with the surface predominantly covered by extensive, thick volcanic lava layers. The exposed strata mainly consist of Lower Paleozoic Ordovician–Silurian systems. The ore bodies occur within the upper section of the Upper Ordovician Formation (O_3l^2) characterized by muddy sandstone, sandstone, and inter-bedded marble layers. The ore bodies primarily exhibit strata-like and lens-like morphologies [14]. The lithology mainly comprises low-grade metamorphic sandstone, mudstone, siltstone, and limestone [22]. The total exposed strata thickness is 2115 m, with a general strike direction of NNE 20° to 30° and a dip angle of 60° to 70° . The overall inclination direction is NWW. The mining area's structure is dominated by faults, exhibiting multidirectional and composite features [28], primarily controlled by the Xinsheng–Longwan backfold and the Fenghuangchong–Lingjiao (overturned) syncline. NE–NNE trending faults are the main ore-controlling structures, forming a distinct NNE-oriented structural belt [22]. The mining area has experienced frequent and long-lasting magmatic activity, resulting in the widespread distribution and diverse types of magmatic rocks, which mainly occur as stocks and dikelets. The granitic porphyry within the study area primarily intrudes the strata and earlier magmatic rocks in a vein-like manner, displaying grayish-white to grayish-black colors, porphyritic textures, and blocky structures (Figure 2). Phenocrysts mainly consist of quartz, feldspar, and hornblende, with grain sizes ranging from 2 to 8 mm and accounting for 30% to 45% of the total rock

volume. Quartz and feldspar phenocrysts exhibit high euhedrality, with some feldspar phenocrysts partially altered by later hydrothermal events. The matrix predominantly comprises fine-grained textures, and accessory minerals include apatite and zircon.

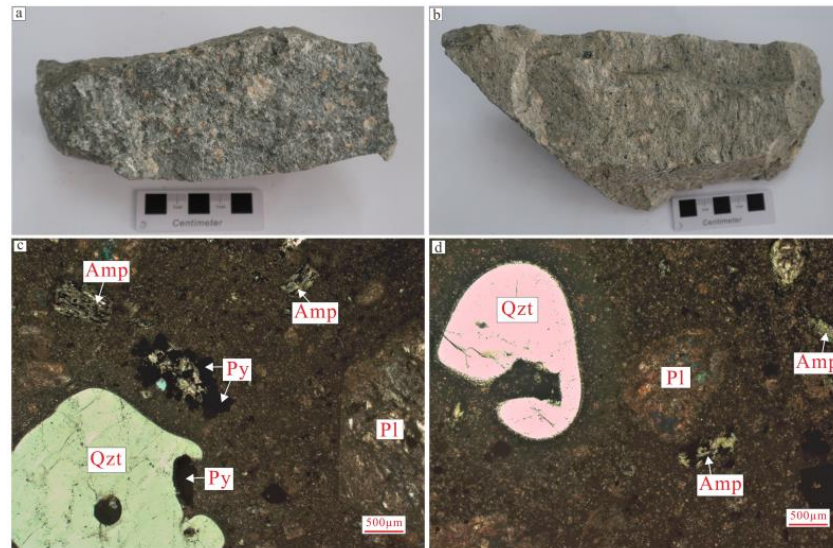


Figure 2. Photographs and photomicrographs of Granitic Porphyry. (a,b) Longwan granite porphyry hand specimen; (c,d) microscopic photograph of granite porphyry. Qzt—Quartz, Amp—Amphibole, Pl—Plagioclase, Py—Pyrite.

The ore body's occurrence is generally consistent with the surrounding rock's occurrence and exhibits a strong association with intrusive bodies and veins. The ore body is characterized by significant thickness, high grades, and frequent limestone inclusions [28]. The mineral assemblage within the ore is relatively simple, with the primary metallic minerals being sphalerite, galena, pyrite, pyrrhotite, chalcopyrite, and magnetite. Non-metallic minerals include quartz, calcite, garnet, chlorite, and glauconite. The ore's structural types are relatively uncomplicated, encompassing euhedral to subhedral granular structures, xenomorphic structures, brecciated structures, replacement structures, and dissolution-residual structures. The ore textures mainly consist of vein-like, disseminated, and blocky structures (Figure 3). The alteration types of the surrounding rocks in the mining area primarily involve skarnization, silicification, and marblization.

Based on the analysis of metal and gangue mineral assemblages, structural features, and interrelationships, the ore deposit can be broadly divided into two mineralization stages and four mineralization phases (Figure 4). (1) Sedimentary-diagenetic stage (initial ore-bearing formation period): During the Early Paleozoic, southeastern Guangxi experienced a tensional fault tectonic environment, which led to the formation of a pyrite-bearing calcareous mudstone. Pyrite commonly exhibits euhedral crystals, predominantly with cubic faces, medium-to-coarse-grained structure, euhedral granular texture, and sparse disseminated structure, displaying sedimentary ore characteristics [29]. (2) Hydrothermal mineralization stage, further subdivided into four mineralization phases: ① Skarn stage: Characterized by weak mineralization, marly limestone underwent hydrothermal alteration, forming skarn-type minerals, such as diopside, tremolite, and garnet, accompanied by a small amount of quartz. ② Early sulfide stage: The primary ore body consists of metallic and gangue minerals. ③ Late sulfide stage: The metallic minerals are primarily pyrite, with minor amounts of galena and sphalerite, and the grains are coarser than those in the earlier stage. ④ Calcite stage: Thin carbonate veins are observed crosscutting the blocky ore, composed of calcite, and minor fine-grained pyrite.

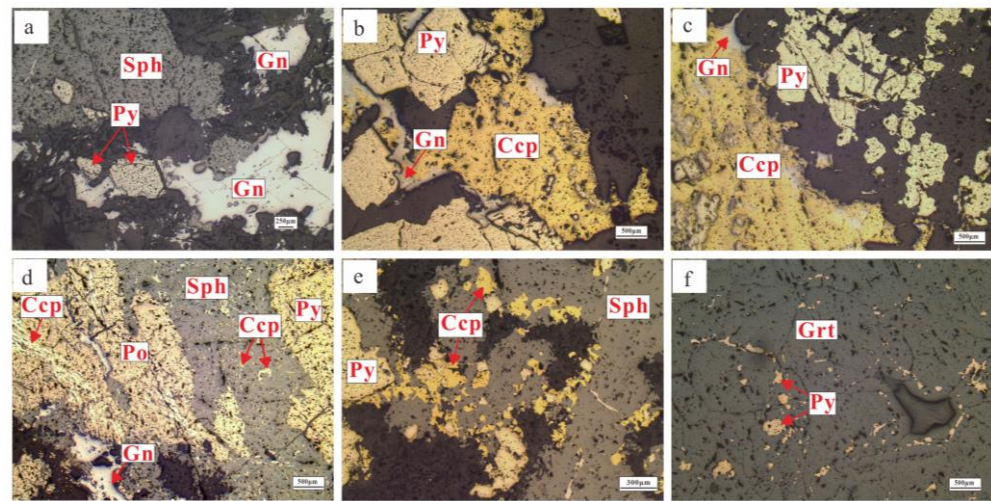


Figure 3. Reflected light photomicrographs of Longwan skarn deposit. (a) Galena replaces early pyrite and is later replaced by galena itself; (b) pyrite appears as euhedral to subhedral granular, while chalcopyrite is anhedral; (c) chalcopyrite and galena coexist, filling the spaces around euhedral pyrite and gangue minerals; (d) sphalerite and galena filled and replaced the early chalcopyrite, pyrite, and Pyrrhotite; (e) chalcopyrite and sphalerite coexist, filling the spaces around pyrite; (f) pyrite and chalcopyrite fill the gaps within garnet crystals. Sph—Sphalerite, Py—Pyrite, Gn—Galena, Ccp—Chalcopyrite, Grt—Garnet, Po—Pyrrhotite.

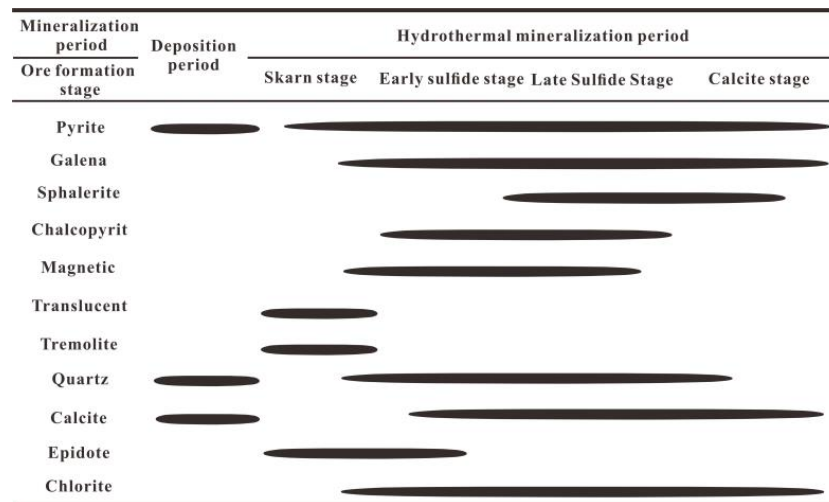


Figure 4. Main mineral formation sequence chart of the Longwan Pb–Zn deposit.

3. Sample Collection and Analytical Methods

3.1. Sample Collection and Description

The granitic porphyry sample (LW-16) utilized for zircon U–Pb dating was obtained from the middle section of 280 (at an elevation of 280 m), along the 60th exploration line. The porphyritic samples are located near the skarn and exhibit a distinct porphyritic texture, making them good representatives of granitic porphyry. This grayish-white rock primarily comprises quartz, plagioclase, and hornblende, with minor chlorite and actinolite as alteration minerals. Under cathodoluminescence, zircon grains within the granitic porphyry display well-defined crystal morphologies, mainly occurring in prismatic and short prismatic shapes. These grains are colorless and transparent and reveal prominent zonal structures in cathodoluminescence images.

Samples (LW-08 and LW-12) used for garnet major element analysis and U–Pb dating were also collected from the Longwan deposit along the 60th exploration line. Both samples represent coarse-grained magnetite–sphalerite garnet skarn (Figure 5) and are products of the alteration stage. The garnets are well-preserved and have not undergone significant post-depositional alteration. The mineral assemblage predominantly consists of garnet, sphalerite, galena, and magnetite. Garnet is yellowish-brown in color, and under microscopic examination, both LW-08 and LW-12 display inconspicuous zoning, lacking evident growth zones in their core regions. They exhibit notable alteration and fracturing, with minor oscillatory zoning along the edges, presenting euhedral to subhedral structures and grain sizes ranging from 1 to 2 cm. Metallic sulfides can be observed within garnet fractures and interstitial spaces between minerals, coexisting with magnetite. Additionally, garnet is altered by later-stage minerals such as diopside and actinolite (Figure 5).

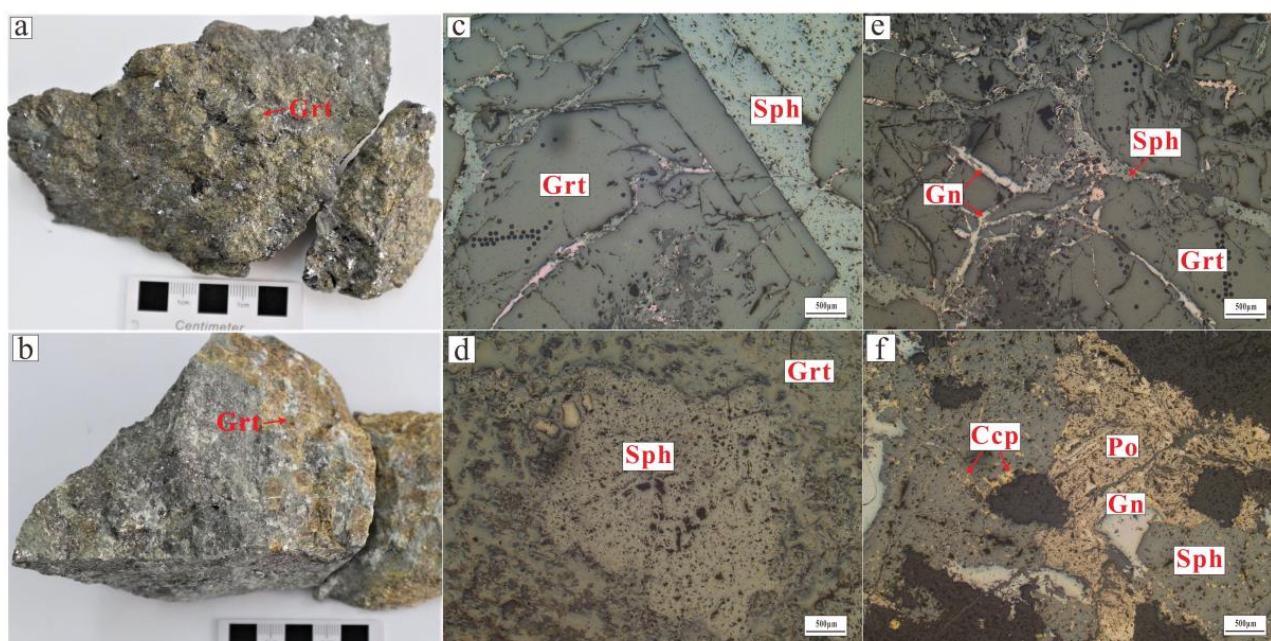


Figure 5. Garnet stone hand specimen and reflected light photomicrographs of Longwan lead–zinc deposit. (a,b) Garnet specimens; (c) sphalerite replaced garnet; (d) sphalerite-replaced garnet; (e) galena occurs as veinlets filling the fractures within garnets; (f) pyrrhotite replacing sphalerite, with chalcopyrite scattered throughout the sphalerite. Sph–Sphalerite, Gn–Galena, Grt–Garnet, Ccp–Chalcopyrite, Po–Pyrrhotite.

3.2. Analytical Methods

Garnet samples for this study were prepared by directly cutting hand specimens into polished thin sections. Following identification under a microscope, representative, unaltered garnet samples devoid of inclusions were chosen for electron probe microanalysis (EPMA) and LA-ICP-MS U–Pb dating. EPMA of garnets’ chemical composition was performed at the Guangxi Key Laboratory of Hidden Metallic Ore Deposits Exploration of the Guilin University of Technology using a JEOL JXA-8230 M Electron Microprobe Analyzer (Japan Electron Optics Laboratory, Tokyo, Japan). We utilized its WDS (wavelength dispersive X-ray spectrometer) function. The instrument settings included an accelerating voltage of 15 kV, a beam current of 20 nA, and a beam diameter of 5 µm. Characteristic peak measurement time for elements was set at 10 s with a background collection time of 5 s. Major elements analyzed comprised SiO₂, Al₂O₃, FeO, MgO, MnO, TiO₂, CaO, Na₂O, K₂O, and P₂O₅, with a detection limit of 0.01% for oxides [30]. Calibrations were conducted using silicate mineral and oxide standards from the American SPI company.

The garnet LA-ICP-MS U–Pb dating test analysis in this study was conducted on an Analytik-Jena PlasmaQuant MS quadrupole ICP-MS at Beijing Yandu Zhongzhi Test Technology Co., Ltd., using a 193 nm NWR193 Ar-F excimer laser. The MALI grandite (U–Pb TIMS = 202.0 ± 1.2 Ma) [31] was employed as the primary standard to calibrate the U–Pb geochronology of garnet. Instrument drift, mass bias, and fractionation of the U–Pb ratio were corrected using a standard-sample bracketing method. Trace element concentrations of garnet were quantified using SRM610 as an external standard and ^{29}Si as the internal standard element, assuming a stoichiometric garnet composition. Each analysis on the garnet began with a 15 s blank gas measurement, followed by an additional 40 s of analysis time when the laser was activated. The laser was operated at 10 Hz, with the beam size set at 55 μm and a density of approximately 3 J/cm². A flow of He carrier gas at a rate of 0.6 L/min carried particles ablated by the laser out of the chamber to be mixed with Ar gas and conveyed to the plasma torch. The isotopes measured included ^{27}Al , ^{29}Si , ^{44}Ca , ^{206}Pb , ^{207}Pb , ^{208}Pb , ^{232}Th , ^{235}U , and ^{238}U , with longer counting times for Pb isotopes compared to other elements. Raw data were corrected offline using ICP-MS-DataCal software (Version 10.9) [32,33] and ZSkits software [34]. Common Pb was corrected using the ^{207}Pb -based correction method outlined in reference [35]. A total of 29 sample points were analyzed for LW-08, with each analysis taking 3 min. The detailed analytical method adhered to the procedures outlined in [36]. Isoplot 4.15 was utilized to calculate U–Pb ages and obtain the lower intercept ages in the Tera-Wasserburg diagram, which can be used as the formation time of common-lead-bearing minerals [33,36].

Zircon selection and cathodoluminescence (CL) imaging were completed at Nanjing Hongchuang Geological Exploration Technology Service Co., Ltd. (Nanjing, China) and LA-ICP-MS U–Pb dating analysis was conducted at the Guangxi Key Laboratory of Hidden Metallic Ore Deposits Exploration of the Guilin University of Technology. The LA-ICP-MS system consisted of a laser and an Agilent 7900 ICP-MS instrument (Agilent, USA). The experimental parameters included a laser beam diameter of 32 μm , a laser frequency of 6 Hz, and an ablation time of 40 s. The standard zircon TEMORA ($^{206}\text{Pb}/^{238}\text{U}$ age of 416.75 ± 0.24 Ma) [37] was utilized as an external standard for zircon U–Pb age analysis. The standard was measured every 5–6 samples to calibrate isotopic fractionation effects in zircon. The GJ-1 zircon standard was interspersed among test samples to verify the accuracy of the analytical method. During testing, the $^{206}\text{Pb}/^{238}\text{U}$ weighted average age for the GJ-1 zircon standard was 603.8 ± 7.3 Ma (2σ , MSWD = 0.51, $n = 5$) (MSWD-mean square of weighted deviates), consistent with the recommended value of 605.4 ± 3.0 Ma (2σ) [38] within the error range. Along with obtaining the U and Pb isotopic ratios, trace element data for zircon were also acquired simultaneously. Zircon trace element concentrations and U–Pb age corrections were performed using the ICPMSDataCal (Version 12.2) program developed by Liu Yongsheng at the China University of Geosciences [39]. Age calculations employed standard zircon TEMORA as an external standard for isotopic ratio fractionation correction, while ^{29}Si was utilized as an internal standard and NIST610 as an external standard for correcting zircon trace element concentrations. Due to the influence of radiogenic Pb isotopes, $^{206}\text{Pb}/^{238}\text{U}$ was used for ages < 1000 Ma. Most of the measured analysis points had $^{206}\text{Pb}/^{204}\text{Pb} > 1000$, and no common Pb correction was applied. ^{204}Pb was detected by an ion counter, and analysis points with abnormally high ^{204}Pb content, potentially influenced by inclusions or other common Pb sources, were excluded from calculations. Sample age data U–Pb concordia diagrams and age distribution diagrams were generated using Ludwig's Isoplot program.

4. Results

4.1. Major Element Compositions of Garnets

Major element analyses of garnet samples LW-08 and LW-12 from the Longwan Pb–Zn deposit are presented in Table 1. Garnets are primarily composed of andradite and grossular solid solution series (Figure 6). Both samples exhibit similar major element compositions. In sample LW-08, SiO_2 content ranges from 32.95% to 36.09%, CaO from

34.99% to 36.25%, Al₂O₃ from 0 to 0.92%, FeO from 26.75% to 30.01%, MnO from 1.06% to 1.39%, and MgO from 0% to 0.04%. The calculated end-member compositions for this garnet are predominantly andradite (96.13% to 100.11%) and grossular (6.51% to 16.09%), with minor contributions from spessartine (0.00% to 0.15%) and almandine (2.57% to 3.36%). In sample LW-12, SiO₂ content ranges from 33.53% to 35.60%, CaO from 35.26% to 36.47%, Al₂O₃ from 0.09% to 1.97%, FeO from 26.07% to 28.82%, MnO from 0.89% to 1.26%, and MgO from 0.01% to 0.16%. The calculated end-member compositions for this garnet are predominantly andradite (91.97% to 99.81%) and grossular (8.28% to 19.11%), with minor contributions from spessartine (0.07% to 0.68%) and almandine (2.25% to 3.10%). SiO₂ (32.95% to 36.09%) and CaO (34.99% to 36.47%) content ranges in all samples exhibit limited variation, while FeO (26.07% to 30.01%) and Al₂O₃ (0 to 1.97%) content show slight variation and display a negative correlation (Figure 7).

Table 1. Electron probe major elements data of representative garnet in the Longwan deposit.

Component	LW-08			LW-12			
	Max	Min	Average (n = 21)	Max	Min	Average (n = 10)	
			wt. %				
SiO ₂	36.09	32.95	34.81	35.60	33.53	34.70	
Al ₂ O ₃	0.92	0.00	0.19	1.97	0.09	0.58	
FeO	30.01	26.75	28.34	28.82	26.07	27.83	
MnO	1.39	1.06	1.19	1.26	0.89	1.10	
MgO	0.04	0.00	0.02	0.16	0.01	0.09	
CaO	36.25	34.99	35.51	36.47	35.26	35.85	
Total	104.69	95.75	100.06	104.27	95.85	100.15	
			Calculated from 12 oxygen atoms				
Si	3.18	3.07	3.15	3.16	3.07	3.12	
Al	0.10	0.00	0.02	0.21	0.01	0.07	
Ti	0.01	0.00	0.00	0.01	0.00	0.00	
Fe ³⁺	2.50	2.22	2.29	2.41	2.13	2.28	
Fe ²⁺	2.22	2.06	2.14	2.17	1.95	2.09	
Mn	0.11	0.08	0.09	0.10	0.07	0.08	
Mg	0.00	0.00	0.00	0.02	0.00	0.01	
Ca	3.56	3.37	3.46	3.46	3.45	3.46	
Total	11.68	10.08	11.15	11.53	10.68	11.12	
Andradite	100.11	96.13	99.15	99.81	91.97	97.61	
Grossular	16.09	6.51	10.17	19.11	8.28	12.92	
Pyrope	0.15	0.00	0.08	0.68	0.07	0.42	
Spessartine	3.36	2.57	2.90	3.10	2.25	2.64	

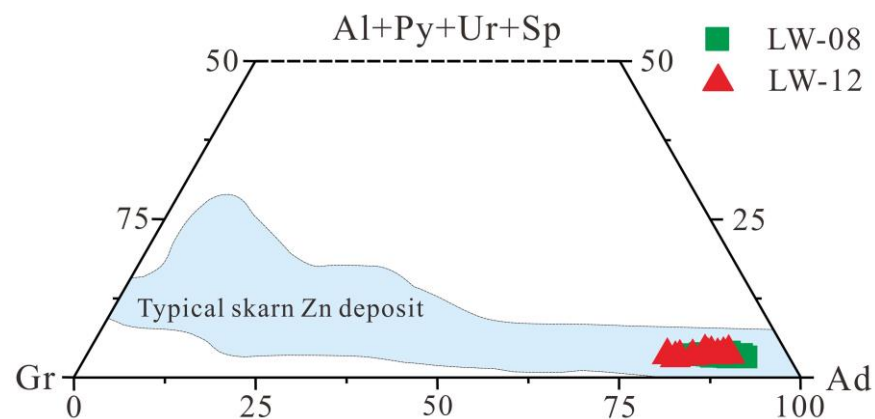


Figure 6. Triangular distribution of garnet samples in the Longwan Pb–Zn deposit (Modified after [40]).

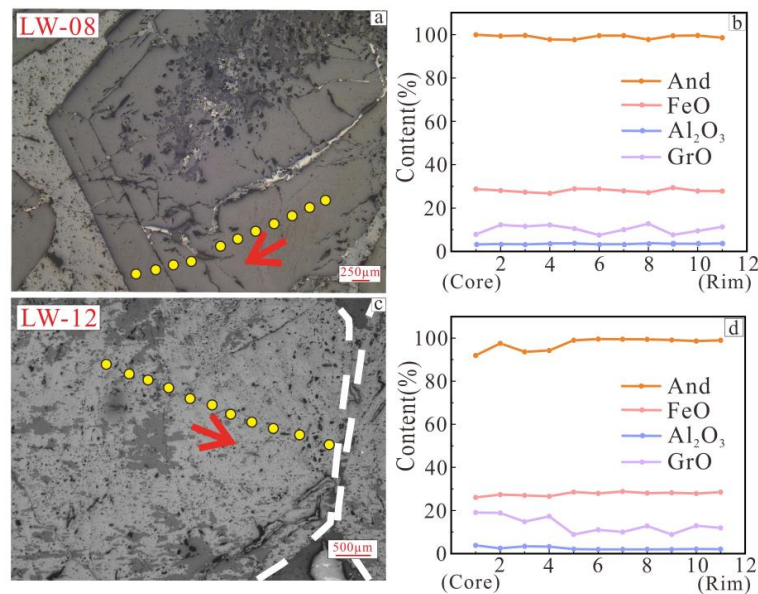


Figure 7. Relative proportions of Adr–Gro and Al₂O₃–TFeO profiles of the garnet particle composition in the ring zone of the Longwan Pb–Zn deposit. (a,b) the variation of the ring-band composition of garnet particles in LW-08; (c,d) the variation of the ring-band composition of garnet particles in LW-12. Additionally, Gro are abbreviations for Andalusite and Grossular.

4.2. LA-ICP-MS U–Pb Isotope Analysis Results of Garnet

Garnets from the Longwan Pb–Zn deposit, as revealed by backscattered images and electron probe analyses, are brown minerals with fracture structures in samples LW-08 and LW-12. Metallic sulfides are observed within garnet fractures and interstitial spaces between minerals. The garnets selected for LA-ICP-MS U–Pb dating mainly come from the LW-08 skarn sample, which features distinct zoning at the edges. The experimental data show that U and Th concentrations in garnets vary considerably, with U concentrations ranging from 0.49 ppm to 3.34 ppm and Th concentrations from 0 to 0.037 ppm (Table 2). The average U concentration in garnets is 1.56×10^{-6} , with andradite as the dominant component followed by grossular. The ²⁰⁷Pb/²⁰⁶Pb and ²³⁸U/²⁰⁶Pb isotope ratios of the samples are plotted on a Concordia diagram, with 29 data points distributed evenly on or near the Concordia curve (Figure 8). The lower intercept age is determined to be 102.4 ± 2.0 Ma (MSWD = 0.74, n = 29).

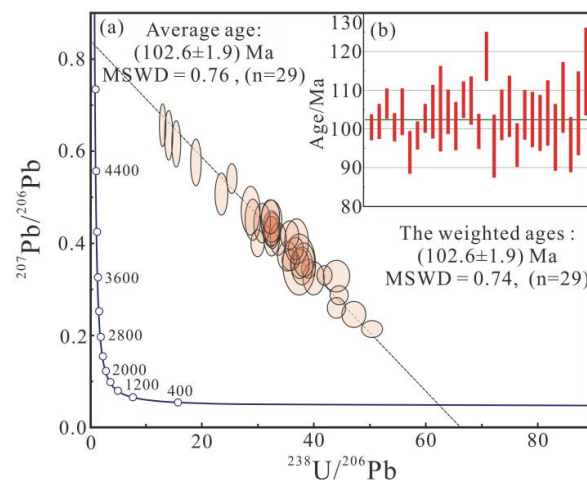


Figure 8. U–Pb age of garnet in skarn of the Longwan Pb–Zn deposit. (a) Tera-Wasserburg diagram and (b) weighted average diagram of ²⁰⁷Pb-corrected ²⁰⁶Pb/²³⁸U age for Longwan garnet.

Table 2. Garnet LA-ICP-MS U–Pb isotope analysis results of the Longwan Pb–Zn Deposit.

Spot No.	ppm		Isotope Ratio						Age/Ma					
	Th	U	²⁰⁷ Pb/ ²⁰⁶ Pb	1σ	²⁰⁷ Pb/ ²³⁵ U	1σ	²⁰⁶ Pb/ ²³⁸ U	1σ	²⁰⁷ Pb/ ²⁰⁶ Pb	1σ	²⁰⁷ Pb/ ²³⁵ U	1σ	²⁰⁶ Pb/ ²³⁸ U	1σ
LM-08-01	0.002	1.41	0.325	0.02	1.12	0.060	0.03	0.0008	3591.4	113	764.50	29	159.80	5
LM-08-02	0.002	0.88	0.471	0.03	2.27	0.114	0.03	0.0014	4154.2	110	1204.30	36	221.70	9
LM-08-05	0.001	1.33	0.373	0.02	1.46	0.080	0.03	0.0009	3801.6	86	914.70	33	180.90	6
LM-08-06	0.002	1.38	0.426	0.02	1.82	0.068	0.03	0.0009	4004.3	77	1054.40	24	197.10	5
LM-08-07	0.002	1.40	0.428	0.03	1.82	0.075	0.03	0.0008	4010.7	90	1052.30	27	195.70	5
LM-08-08	0.002	1.40	0.401	0.02	1.85	0.078	0.03	0.0009	3912.2	73	1064.50	28	212.60	6
LM-08-09	0.001	1.45	0.433	0.03	1.85	0.079	0.03	0.0010	4029	86	1063.10	28	196.50	6
LM-08-10	0.001	1.41	0.418	0.02	1.62	0.073	0.03	0.0009	3976.2	73	979.10	28	178.90	5
LM-08-11	0.002	1.38	0.329	0.02	1.03	0.055	0.02	0.0008	3612.6	106	720.40	27	145.10	5
LM-08-13	0.001	1.35	0.410	0.02	1.69	0.074	0.03	0.0008	3944.7	85	1003.20	28	189.60	5
LM-08-14	0.001	1.36	0.364	0.02	1.32	0.069	0.03	0.0009	3768.1	102	853.70	30	167.00	5
LM-08-16	0.002	0.96	0.354	0.04	1.31	0.124	0.03	0.0014	3726.2	188	851.10	54	170.80	9
LM-08-17	0.000	0.99	0.404	0.03	1.52	0.092	0.03	0.0010	3925.5	121	936.70	37	172.90	7
LM-08-18	0.006	1.33	0.452	0.03	2.15	0.105	0.03	0.0011	4091.1	97	1165.40	34	218.80	7
LM-08-19	0.001	1.35	0.351	0.03	1.28	0.069	0.03	0.0009	3712.4	117	837.90	31	168.50	6
LM-08-21	0.002	1.08	0.416	0.03	1.77	0.089	0.03	0.0009	3967.7	102	1035.90	33	196.40	6
LM-08-23	0.003	1.14	0.449	0.03	1.92	0.089	0.03	0.0012	4080.8	101	1086.90	31	196.70	7
LM-08-28	0.028	0.78	0.444	0.03	2.00	0.105	0.03	0.0011	4066.5	95	1115.30	36	207.00	7
LM-08-39	0.013	0.77	0.508	0.03	3.00	0.136	0.04	0.0014	4263.2	87	1406.50	35	270.20	9
LM-08-40	0.008	3.34	0.364	0.01	1.40	0.060	0.03	0.0008	3765.2	62	890.40	25	178.00	5
LM-08-41	0.021	2.92	0.246	0.02	0.72	0.054	0.02	0.0006	3159.4	120	551.60	32	135.70	4
LM-08-42	0.014	3.02	0.288	0.01	0.89	0.035	0.02	0.0005	3404.8	75	648.20	19	143.60	3
LM-08-43	0.015	1.87	0.458	0.02	1.97	0.107	0.03	0.0010	4111.6	79	1103.80	37	197.60	7
LM-08-44	0.037	2.39	0.260	0.01	0.82	0.035	0.02	0.0006	3248	90	606.40	20	145.10	4
LM-08-45	0.002	3.26	0.345	0.01	1.22	0.047	0.03	0.0005	3685.8	60	811.60	22	163.70	3
LM-08-46	0.005	1.66	0.356	0.02	1.32	0.067	0.03	0.0008	3734.4	91	852.50	29	170.30	5
LM-08-47	0.002	2.16	0.389	0.02	1.46	0.057	0.03	0.0007	3867.6	62	915.80	23	173.60	4
LM-08-49	0.008	3.05	0.331	0.01	1.09	0.041	0.02	0.0005	3621.1	65	749.30	20	152.40	3
LM-08-50	0.016	2.94	0.214	0.01	0.59	0.031	0.02	0.0005	2936.6	92	469.00	20	127.00	3

4.3. LA-ICP-MS U–Pb Dating Results of Zircons

Zircon crystals in the granitic porphyry of the Longwan Pb–Zn deposit are well-formed, mainly exhibiting elongated and short prismatic shapes, and are colorless and transparent. Cathodoluminescence images show distinct zoning in the zircons. The LA-ICP-MS U–Pb dating results for zircons (Table 3) reveal U concentrations ranging from 950 ppm to 1760 ppm and Th concentrations from 179.1 ppm to 949.6 ppm. The Th/U ratios of zircons mainly vary between 0.17 and 0.61 ppm (average 0.40). Excluding a few samples, the Th/U ratios are all greater than 0.3, indicating a magmatic origin for the zircons. In this study, zircons from the granitic porphyry in close contact with the skarn were obtained through 20 data points. These points are all located on or near the Concordia curve on the Concordia diagram, yielding a weighted average age of 102.1 ± 1.2 Ma (MSWD = 0.26, n = 20) (Figure 9).

Table 3. LA-ICP-MS U–Pb zircon analysis data of granite-porphyry in the Longwan Pb–Zn Deposit.

Spot No.	ppm			Th/U	Isotope Ratio						Age/Ma					
	Th	U			²⁰⁷ Pb/ ²⁰⁶ Pb	1σ	²⁰⁷ Pb/ ²³⁵ U	1σ	²⁰⁶ Pb/ ²³⁸ U	1σ	²⁰⁷ Pb/ ²⁰⁶ Pb	1σ	²⁰⁷ Pb/ ²³⁵ U	1σ	²⁰⁶ Pb/ ²³⁸ U	1σ
LW-16-01	794.54	1645.89	0.48	0.0521	0.0027	0.1148	0.0062	0.0159	0.0004	300	149	110	6	102	2	
LW-16-03	466.87	1273.65	0.37	0.0470	0.0023	0.1010	0.0048	0.0158	0.0003	56	111	98	4	101	2	
LW-16-04	613.44	1760.37	0.35	0.0492	0.0021	0.1102	0.0054	0.0162	0.0004	167	98	106	5	104	3	
LW-16-05	599.73	1556.85	0.39	0.0492	0.0021	0.1075	0.0048	0.0161	0.0004	167	102	104	4	103	3	
LW-16-07	323.25	1055.83	0.31	0.0473	0.0029	0.1030	0.0070	0.0156	0.0004	65	146	100	6	100	3	
LW-16-09	484.09	1356.38	0.36	0.0481	0.0023	0.1088	0.0063	0.0162	0.0006	106	107	105	6	104	4	
LW-16-11	838.38	1608.91	0.52	0.0472	0.0021	0.1021	0.0054	0.0160	0.0006	58	104	99	5	102	4	
LW-16-12	386.89	1274.58	0.30	0.0463	0.0020	0.1014	0.0050	0.0163	0.0006	9	113	98	5	104	4	
LW-16-14	688.09	1760.77	0.39	0.0491	0.0021	0.1075	0.0050	0.0157	0.0003	154	103	104	5	100	2	
LW-16-16	561.01	1685.58	0.33	0.0479	0.0023	0.1068	0.0053	0.0161	0.0004	98	107	103	5	103	2	
LW-16-18	605.52	1100.01	0.55	0.0477	0.0026	0.1015	0.0054	0.0160	0.0005	83	126	98	5	102	3	
LW-16-19	652.70	1654.61	0.39	0.0472	0.0022	0.1003	0.0047	0.0156	0.0004	58	107	97	4	100	2	
LW-16-20	179.10	1074.91	0.17	0.0439	0.0021	0.0966	0.0054	0.0160	0.0005	-	-	94	5	102	3	
LW-16-21	581.77	950.49	0.61	0.0489	0.0031	0.1064	0.0069	0.0162	0.0006	146	141	103	6	104	4	
LW-16-22	568.28	1246.50	0.46	0.0470	0.0025	0.1033	0.0063	0.0162	0.0005	56	113	100	6	103	3	
LW-16-23	236.28	995.77	0.24	0.0478	0.0027	0.1050	0.0062	0.0161	0.0006	100	120	101	6	103	4	
LW-16-24	641.59	1702.33	0.38	0.0505	0.0023	0.1093	0.0055	0.0160	0.0006	220	107	105	5	102	4	
LW-16-25	394.91	841.16	0.47	0.0545	0.0033	0.1173	0.0068	0.0163	0.0006	391	135	113	6	104	4	
LW-16-27	399.93	1259.69	0.32	0.0464	0.0023	0.0979	0.0048	0.0159	0.0004	17	115	95	4	102	3	
LW-16-31	949.58	1544.68	0.61	0.0510	0.0028	0.1105	0.0058	0.0161	0.0003	243	126	106	5	103	2	

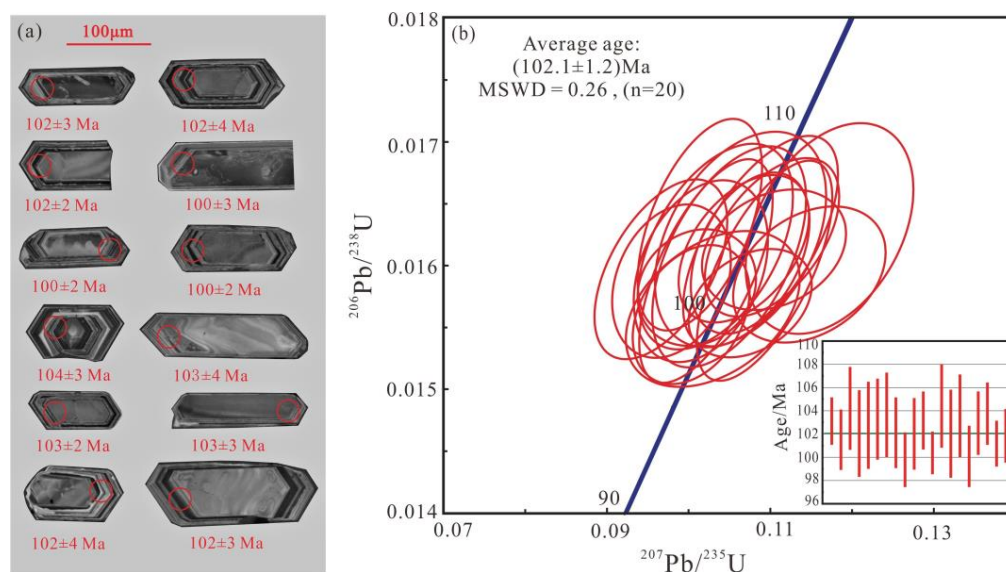


Figure 9. Zircon U–Pb ages of granitic porphyry in the Longwan Pb–Zn deposit. (a) Representative cathodoluminescent images of analyzed zircon spots and (b) Zircon U–Pb Concordia diagram for granitic porphyry, also shown is the weighted mean ages.

5. Discussion

5.1. Formation Age of the Longwan Pb–Zn Deposit

The Longwan Pb–Zn deposit is an important deposit within the Fozichong mining district, with great exploration potential. Previous studies have carried out K–Ar and Rb–Sr dating on Longwan granites (Table 4); however, these methods can be easily influenced by subsequent magmatic and tectonic activities, possibly affecting dating results [39]. Zircon U–Pb dating from previous research suggests an age of 104.2 Ma for the Longwan monzogranite porphyry. However, in the skarn deposits, intrusive bodies often do not spatially contact the skarns, rendering the age of the intrusion insufficient for directly indicating the mineralization age. Garnet is a common alteration mineral in skarn deposits, characterized by high closure temperature ($>850\text{ }^{\circ}\text{C}$), stability, and limited influence by subsequent magmatic-hydrothermal and tectonic activities [5]. Garnet can better constrain the timing of metamorphic events and subsequently the formation age of skarn deposits, making it an ideal mineral for dating skarn deposits.

Table 4. Age table of the Longwan Pb–Zn deposit.

Minerals	Methods	Age	Source
Potassium feldspar in the Longwan rock mass	K–Ar	75.5 Ma	[23]
Longwan Erchang granite porphyry whole rock	Rb–Sr isochrones	127.6 Ma	[29]
Longwan Erchang granite porphyry	LA–ICP–MS U–Pb	104.2 ± 1.5 Ma	[13]
Guyi Erchang granite porphyry	LA–ICP–MS U–Pb	105.1 ± 1.7 Ma	[13]
Hesan Second-length granite porphyry	LA–ICP–MS U–Pb	105.2 ± 0.5 Ma	[13]
Longwan granite porphyry	LA–ICP–MS U–Pb	102.1 ± 1.2 Ma	This study
Longwan Garnet	LA–ICP–MS U–Pb	102.6 ± 1.9 Ma	This study

Garnet can be classified into grossular ($\text{Ca}_3\text{Al}_2\text{Si}_3\text{O}_{12}$), andradite ($\text{Ca}_3\text{Fe}_2\text{Si}_3\text{O}_{12}$), almandine ($\text{Fe}_3\text{Al}_2\text{Si}_3\text{O}_{12}$), pyrope ($\text{Mg}_3\text{Al}_2\text{Si}_3\text{O}_{12}$), and spessartine ($\text{Mn}_3\text{Al}_2\text{Si}_3\text{O}_{12}$), based on differences in primary chemical compositions. The most commonly occurring garnet in skarn deposits is the solid solution of grossular and andradite. In the Longwan Pb–Zn deposit, the main garnet series is andradite–grossular (Figure 6). Ore minerals such as galena, sphalerite, and chalcopyrite in the Longwan Pb–Zn deposit fill the interiors or interstices between garnet mineral grains (Figure 3f), indicating a close genetic relationship

and formed during the same fluid evolution process. Experimental studies have shown that only grossular garnets possess a highly homogeneous U distribution, and they contain higher U concentrations than other garnet types [41]. U–Pb isotope analysis results show that the LW-08 garnet samples possess high U concentrations (0.49 ppm to 3.34 ppm), meeting the requirements for garnet U–Pb isotope dating methods. Consequently, the U–Pb isotope dating results from sample LW-08, collected from the skarn within the Longwan Pb–Zn deposit, can represent the mineralization age of the deposit.

The obtained garnet U–Pb age of 102.6 ± 1.9 Ma in this study is consistent with the zircon U–Pb age of 102.1 ± 1.2 Ma from the granitic porphyry within the Longwan deposit and the previously reported zircon U–Pb age of 104.2 ± 1.5 Ma for the Longwan monzogranite porphyry [12]. This consistency suggests that the garnet U–Pb age obtained in this study is reliable and represents the mineralization age of the Longwan Pb–Zn deposit. In recent years, the method of using garnet for geochronological studies of skarn deposits has gained increasing recognition [42,43] and has been more widely applied [9,11], particularly in areas with multiple episodes of skarn activity and a lack of exposed intrusive bodies, where it has demonstrated good application results [10]. During the Late Early Cretaceous, the Longwan Pb–Zn deposit formed through contact metasomatic reactions that occurred during the intrusion of granitic porphyry into the Silurian limestone. The ore-forming process was a continuous event in the temporal scale, closely associated with magmatic evolution. Therefore, this study provides important geochronological evidence for determining the mineralization age and genesis of the Longwan Pb–Zn deposit.

5.2. Tectonic Setting of the Longwan Pb–Zn Deposit

The extensive distribution and diverse types of Cretaceous magmatic rocks in south-eastern Guangxi establish this region as an ideal location for investigating the genesis and tectonic setting of Late Mesozoic magmatic activities in South China. The area lies within the transitional zone between the South China Pacific tectonic domain and the Tethys tectonic domain, situated at the southwestern end of the significant multi-metallic mineralization belt of South China, the Qin-Hang suture belt. Late Mesozoic volcanic rocks, predominantly from the Yanshanian period, are exposed in this region. These magmatic rocks are primarily acidic to intermediate in composition, encompassing biotite granites, granitic porphyries, and granite-porphyries, among others. The zircon and garnet U–Pb ages obtained in this study for the Longwan granitic porphyry and skarn are 102.1 ± 1.2 Ma and 102.6 ± 1.9 Ma, respectively, representing the formation age of the Longwan Pb–Zn deposit. These ages are consistent with the formation times of other intrusions in the southeastern Guangxi region, such as the Xinzhoutang intrusion (98.5–100.5 Ma), Daye volcanic rocks (99.2 Ma) [44], Liuwang quartz porphyry (98.72 ± 0.64 Ma) [15], Luchuan monzogranite (107.6 ± 1.2 Ma) [45], and Guantian granite (98 Ma) [46]. All these rock bodies formed during the Late Early Cretaceous to Early Late Cretaceous period (<110 Ma).

Previous research indicates that during the Late Cretaceous, the Pacific Plate underwent northwestward subduction. Some scholars argue that, between the Early and Late Cretaceous transition (107–86 Ma), the South China Block experienced an extensional phase due to the southeastward rollback of the Pacific Plate [47–49]. The magmatic rocks' ages reveal a progressively younger trend towards the southeast coast, where the magmatic belt exhibits a NE orientation [24]. Consequently, the genesis of the NE-trending magmatic rocks along the southeast coast is thought to be associated with the southeastward rollback of the Pacific Plate [50,51]. The Longwan Pb–Zn deposit is situated relatively far from the NE-trending magmatic belt along the southeast coast, suggesting it may not be influenced by the Pacific tectonic domain. In southern South China, an EW-trending magmatic belt spans Guangdong and Guangxi provinces, extending westward to Yunnan. The ages of these rocks predominantly range from 110 to 80 Ma, with no apparent trend of decreasing age towards the southeast coast [50–52]. Numerous magmatic rocks, including the Longwan granitic porphyry with ages younger than 110 Ma, are positioned within the EW-trending magmatic belt in southern South China. Observations of the spatial distribution of

Cretaceous magmatic rocks in the South China Block reveal that the EW-trending magmatic belt from the Middle-Late Cretaceous (younger than 110 Ma) intersects at a large angle with the contemporaneous NE-trending magmatic belt along the southeast coast [51]. The South China Block's tectonic environment during the Cretaceous underwent multiple episodes of extension and compression [53–59]. Based on the reconstruction of the Pacific Plate's drift history, earlier researchers have proposed that the genesis of the EW-trending granites in South China during the Late Cretaceous is related to the northward subduction of the Neo-Tethys Ocean [51]. They have proposed a model involving northward subduction of the Neo-Tethys plate, ridge subduction, and slab rollback [51,60]. Other scholars have also suggested that the formation of granites and andesites in southeastern Guangxi around 100 Ma is connected to the northward subduction of the Neo-Tethys plate [45,59,61]. The Shilu intrusion (103.9 Ma) within the Yangchun Basin displays adakitic features and may have been formed through partial melting of the slab during the northward subduction of the Neo-Tethys Ocean [51]. Sr-Nd isotopic analysis of the monzogranitic porphyries from the Longwan Pb–Zn deposit has demonstrated that their source region is crustal [14], differing from the Shilu intrusion's origin and not being a product of oceanic crust partial melting.

At approximately 100 Ma, magmatic activity was present from the northeast to the southwest along the southern segment of the Qin-Hang metallogenic belt. In the Huaiji Basin, located about 100 km northeast of Longwan, 102 Ma volcanic rocks have been identified [62]. The Fozichong granitic porphyry near Longwan has a formation age of 100 Ma, the Jinzhu dacite is dated at 98.1 Ma, the Liuwang quartz porphyry 98 Ma is situated 50 km southwest of Longwan [16], and the Xinzhoutang andesite, 150 km southwest of Longwan, has an age range of 98.5–100.5 Ma [47]. These magmatic rocks are predominantly distributed along a NE–SW axis along the Cenxi-Bobai Fault, suggesting extensive magmatic activity around 100 Ma during the mid-Cretaceous along this fault. Evidence such as the deceleration of the Indian Plate's drift rate, the emergence of adakitic rocks, and plate reconstructions point to the Neo-Tethys ridge subducting beneath southern South China around 100 Ma [51,60]. With the increase in subduction angle, slab rollback transpired, establishing an NS-trending extensional tectonic regime in southern South China. This incited the activation of the southern section of the Qin-Hang metallogenic belt, giving rise to a series of magmatic events. Concurrently, as the slab retreated southward, a pattern of progressively younger magmatic evolution from north to south materialized, aligning with the age variation trend of volcanic rocks from the Huaiji Basin (102 Ma) to the Daban Basin (94 Ma) and the Shuiwen Basin (82 Ma) [62]. The Longwan Pb–Zn deposit is situated within the Cenxi-Bobai Fault zone, in the southwestern segment of the Qin-Hang metallogenic belt [16,63]. The Late Cretaceous granitic porphyry associated with the Longwan Pb–Zn deposit may have formed during the reactivation of the NE-trending Cenxi-Bobai Fault under the context of the Neo-Tethys plate rollback. This process facilitated the generation of a series of NE-trending Pb–Zn deposits in the southwestern section of the Qin-Hang metallogenic belt, including the Longwan, Jilongding, Longjing, and Dongtao Pb–Zn deposits (Figure 10).

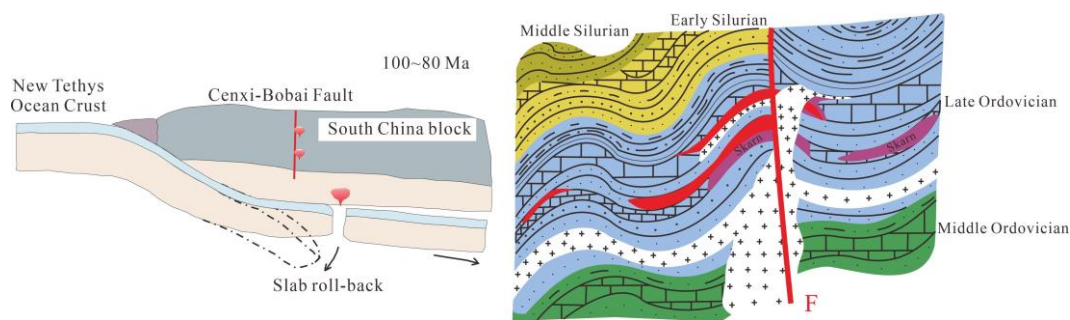


Figure 10. Conceptual diagram illustrating the tectonic and ore-forming evolution of the Longwan lead–zinc deposit during the early Late Cretaceous (~100–80 Ma).

6. Conclusions

By conducting U–Pb dating on garnet from skarn within the Longwan Pb–Zn deposit and zircon from granitic porphyry, we obtained a garnet U–Pb age of 102.6 ± 1.9 Ma, representing the mineralization epoch of the Longwan Pb–Zn deposit. This age signifies that the formation of the Longwan Pb–Zn deposit involved a continuous process of magmatic evolution and mineralization. The consistency between U–Pb ages of garnet in the skarn and zircon in the granitic porphyry validates the accuracy of garnet dating in constraining the mineralization age of skarn-type deposits. Considering previous research, this study suggests that the geodynamic setting of the Longwan Pb–Zn deposit is associated with the northward subduction of the Neo-Tethys Ocean. The extensive magmatic activity along the southern segment of the Qin-Hang metallogenic belt around 100 Ma during the mid-Cretaceous correlates with the geological process of the Neo-Tethys ridge subducting beneath southern South China at approximately 100 Ma, followed by the subsequent slab rollback, which led to an extensional tectonic background.

Author Contributions: Investigation, formal analysis, writing—original draft, X.Z.; methodology, supervision, writing—review and editing, W.D.; writing—review and editing, L.M., W.F., X.L. and S.L. All authors have read and agreed to the published version of the manuscript.

Funding: This research was funded by the National Natural Science Foundation of China (92162218, 42262026), the Guangxi Natural Science Foundation (2022GXNSFBA035588), and the Guangxi Science Innovation Base Construction Foundation (GuikeZY21195031).

Data Availability Statement: The data presented in this study are available on reasonable request from the corresponding authors.

Acknowledgments: We express our sincere gratitude to the geologists of the Longwan Pb–Zn Deposit for their valuable support and assistance during the fieldwork. Special thanks go to Qijun Yang and Jinbao Yang from Guilin University of Technology for their insightful comments and suggestions on the initial manuscript. We are also grateful to Hongxia Yu and Zhenglin Li from the Guangxi Key Laboratory of Hidden Metallic Ore Deposits Exploration at Guilin University of Technology for their expert guidance and help during the experimental process. Finally, we are thankful for the constructive feedback provided by two anonymous reviewers, which has greatly improved the quality of our manuscript. This is a contribution to Guangxi Key Mineral Resources Deep Exploration Talent Highland.

Conflicts of Interest: The authors declare no conflict of interest.

References

1. Zhang, Y.; Shao, Y.J.; Zhang, R.Q.; Li, D.F.; Liu, Z.F.; Chen, H.Y. Dating ore deposit using garnet U–Pb geochronology: Example from the Xinqiao Cu–S–Fe–Au deposit, Eastern China. *Minerals* **2018**, *8*, 31. [\[CrossRef\]](#)
2. Jamtveit, B.; Ragnarsdottir, K.V.; Wood, B.J. On the origin of zoned grossular-andradite garnets in hydrothermal systems. *Eur. J.* **1995**, *7*, 1399–1410. [\[CrossRef\]](#)
3. Gaspar, M.; Knaack, C.; Meinert, L.D.; Moretti, R. REE in skarn systems: A LA-ICP-MS study of garnets from the Crown Jewel gold deposit. *Geochim. Cosmochim. Acta* **2008**, *72*, 185–205. [\[CrossRef\]](#)

4. Baghban, S.; Hosseinzadeh, M.R.; Moayyed, M.; Mokhtari, M.A.A.; Gregory, D.D.; Mahmoudi, N.H. Chemical composition and evolution of the garnets in the Astamal Fe-LREE distal skarn deposit, Qara-Dagh-Sabalan metallogenic belt, Lesser Caucasus, NW Iran. *Ore Geol. Rev.* **2016**, *78*, 166–175. [[CrossRef](#)]
5. Mezger, K.; Hanson, G.N.; Bohlen, S.R. U–Pb systematics of garnet: Dating the growth of garnet in the late Archean Pikwitonei granulite domain at Cauchon and Natawahunan Lakes, Manitoba, Canada. *Contrib. Miner. Petrol.* **1989**, *101*, 136–148. [[CrossRef](#)]
6. Gevedon, M.; Semen, S.; Barnes, J.D.; Lackey, J.S.; Stockli, D.F. Unraveling histories of hydrothermal systems via U–Pb laser ablation dating of skarn garnet. *Earth Planet. Sci. Lett.* **2018**, *498*, 237–246.
7. Li, D.F.; Tan, C.Y.; Miao, F.Y.; Liu, Q.F.; Zhang, Y.; Sun, X.M. Initiation of Zn–Pb mineralization in the Pingbao Pb–Zn skarn district, South China: Constraints from U–Pb dating of grossular-rich garnet. *Ore Geol. Rev.* **2019**, *107*, 587–599. [[CrossRef](#)]
8. Tang, Y.W.; Gao, J.F.; Lan, T.G.; Cui, K.; Han, J.J.; Zhang, X.; Chen, Y.W.; Chen, Y.H. In situ low-U garnet U–Pb dating by LA-SF-ICP-MS and its application in constraining the origin of Anji skarn system combined with Ar–Ar dating and Pb isotopes. *Ore Geol. Rev.* **2021**, *130*, 103970. [[CrossRef](#)]
9. Deng, X.D.; Li, J.W.; Luo, T.; Wang, H.Q. Dating magmatic and hydrothermal processes using andradite-rich garnet U–Pb geochronometry. *Contrib. Miner. Petrol.* **2017**, *172*, 71–82. [[CrossRef](#)]
10. Reinhardt, N.; Gerdes, A.; Beranoaguirre, A.; Frenzel, M.; Meinert, L.D.; Gutzmer, J.; Burisch, M. Timing of magmatic-hydrothermal activity in the Variscan Orogenic Belt: LA-ICP-MS U–Pb geochronology of skarn-related garnet from the Schwarzenberg District, Erzgebirge. *Miner. Depos.* **2022**, *57*, 1071–1087. [[CrossRef](#)]
11. Zang, Z.J.; Dong, L.L.; Liu, W.; Zhao, H.; Wang, X.S.; Cai, K.D.; Wan, B. Garnet U–Pb and O isotopic determinations reveal a shear-zone induced hydrothermal system. *Sci. Rep.* **2019**, *9*, 10382. [[CrossRef](#)] [[PubMed](#)]
12. Yang, Q.J.; Qin, Y.; Wang, T.S.; Zhang, Q.W. Geochronology and Geochemistry Characteristics of Monzo-granitic porphyry from Fozichong ore field Guangxi Province and their geological implication. *J. Jilin Univ. (Earth Sci. Ed.)* **2017**, *47*, 760–774, (In Chinese with English Abstract).
13. Maleki, S.; Alirezaei, S.; Corfuc, F. Dating of Oligocene granitoids in the KhakSorkh area, Central Urumieh-Dokhtar arc, Iran, and a genetic linkage with the associated skarn iron deposit. *J. Asian Earth Sci.* **2019**, *182*, 103930. [[CrossRef](#)]
14. Fu, W.; Chai, M.C.; Yang, Q.J.; Wei, L.M.; Huang, X.R.; Feng, J.P. Genesis of the Fozichong Pb–Zn polymetallic deposit: Constraints from fluid inclusions and H–O–S–Pb isotopic evidences. *Acta Petrol. Sin.* **2013**, *29*, 4136–4150, (In Chinese with English Abstract).
15. Liu, X.Y. Petrogenesis of Late Mesozoic Granites in Southeastern Guangxi and Their Geodynamic Implications. Master’s Thesis, Guilin University of Technology, Guilin, China, 2022.
16. Yu, P.P.; Zheng, Y.; Huang, X.; Wang, C.M. Stratabound skarn Pb–Zn mineralization in the Yunkai Domain (South China): The Fozichong case. *Ore Geol. Rev.* **2020**, *125*, 103673. [[CrossRef](#)]
17. Yu, P.P.; Zheng, Y.; Zhou, Y.Z.; Chen, B.H.; Niu, J.; Yang, W. Zircon U–Pb geochronology and geochemistry of the metabasite and gabbro: Implications for the Neoproterozoic and Paleozoic tectonic settings of the Qinzhou Bay–Hangzhou Bay suture zone, South China. *Geol. J.* **2018**, *53*, 2219–2239. [[CrossRef](#)]
18. Wang, Y.J.; Fan, W.M.; Zhang, G.W.; Zhang, Y.H. Phanerozoic tectonics of the South China Block: Key observations and controversies. *Gondwana Res.* **2013**, *23*, 1273–1305. [[CrossRef](#)]
19. Cheng, S.B.; Fu, J.M.; Ma, L.Y.; Chen, X.Q.; Lu, Y.Y. Zircon SHRIMP U–Pb Dating of Dachong Granodioritic Stock and Its geological significance in Fozichong Deposit, Guangxi Province. *Geol. Miner. Resour. South China* **2012**, *28*, 315–320, (In Chinese with English Abstract).
20. Hu, R.Z.; Zhou, M.F. Multiple Mesozoic mineralization events in South China: An introduction to the thematic issue. *Miner. Depos.* **2012**, *47*, 579–588. [[CrossRef](#)]
21. Mao, J.W.; Cheng, Y.B.; Chen, M.H.; Franco, P. Major types and time-space distribution of Mesozoic ore deposits in South China and their geodynamic settings. *Miner. Depos.* **2013**, *48*, 267–294.
22. Lei, L.Q. Age and Geochemical character of magmatites in Fozichong Pb–Zn (Ag) ore field, Guangxi, China. *Acta Petrol. Sin.* **1995**, *11*, 77–82, (In Chinese with English Abstract).
23. Wang, C.M.; Deng, J.; Carraza, E.J.M.; Lai, X.R. Nature, diversity and temporal-spatial distributions of sediment-hosted Pb–Zn deposits in China. *Ore Geol. Rev.* **2014**, *56*, 327–351. [[CrossRef](#)]
24. Li, X.H.; Zhou, H.W.; Liu, Y.; Lee, C.Y.; Sun, M.; Chen, C.H. Shoshonitic intrusive suite in SE Guangxi: Petrology and geochemistry. *Chin. Sci. Bull.* **2000**, *45*, 653–659. [[CrossRef](#)]
25. Zheng, W.; Mao, J.W.; Pirajno, F.; Zhao, H.J.; Zhao, C.S.; Mao, Z.H.; Wang, Y.J. Geochronology and geochemistry of the Shilu Cu–Mo deposit in the Yunkai area, Guangdong province, South China and its implication. *Ore Geol. Rev.* **2015**, *67*, 382–398. [[CrossRef](#)]
26. Wang, Y.J.; Fan, W.M.; Cawood, P.A.; Ji, S.C.; Peng, T.P.; Chen, X.Y. Indosinian high-strain deformation for the Yunkaidashan tectonic belt, South China: Kinematics and $^{40}\text{Ar}/^{39}\text{Ar}$ geochronological constraints. *Tectonics* **2007**, *26*, 1–21. [[CrossRef](#)]
27. Liu, X.Y. The Subduction of the Tethyan Ocean Beneath the South China Continent in Late Cretaceous: Evidences from the Liuwang Quartz Porphyry in the Southeastern Guangxi. *Bull. Mineral. Petro. Geochem.* **2022**, *41*, 374–387, (In Chinese with English Abstract).
28. Zhai, L.N.; Wang, J.H.; Wei, C.S.; Jiang, H.; Cai, J.H. Researching on the Age of rock-forming and metallogenic epoch of Fozichong ore field in Guangxi. *Geol. Miner. Resour. South. China* **2008**, *95*, 46–49, (In Chinese with English Abstract).

29. He, X.R.; Chen, A.B.; Xie, X.M. Ore Minerals Fabric and Mineralization Stage Division of Pb–Zn Deposit Longwan Guangxi. *Henan Sci.* **2014**, *32*, 1571–1575, (In Chinese with English Abstract).
30. Fan, X.; Wang, X.; Lü, X.; Wei, W.; Chen, W.; Yang, Q. Garnet composition as an indicator of skarn formation: LA-ICP-MS and EPMA studies on oscillatory zoned garnets from the Haobugao skarn deposit, Inner Mongolia. *China. Geol. J.* **2018**, *54*, 1976–1992. [[CrossRef](#)]
31. Seman, S.; Stockli, D.F.; McLean, N.M. U–Pb geochronology of grossular-andradite garnet. *Chem. Geol.* **2017**, *460*, 106–116. [[CrossRef](#)]
32. Liu, Y.S.; Hu, Z.C.; Gao, S.; Gunther, D.; Xu, J.; Gao, C.G.; Chen, H.H. In situ analysis of major and trace elements of anhydrous minerals by LA-ICP-MS without applying an internal standard. *Chem. Geol.* **2008**, *257*, 34–43. [[CrossRef](#)]
33. Liu, Y.S.; Gao, S.; Hu, Z.C.; Gao, C.G.; Zong, K.Q.; Wang, D. Continental and Oceanic Crust Recycling-induced Melt–Peridotite Interactions in the Trans-North China Orogen: U–Pb Dating, Hf Isotopes and Trace Elements in Zircons from Mantle Xenoliths. *J. Petro* **2010**, *51*, 537–571. [[CrossRef](#)]
34. Cai, P.R.; Wang, T.; Wang, Z.Q.; Li, L.M.; Jia, J.L.; Wang, M.Q. Geochronology and geochemistry of late Paleozoic volcanic rocks from eastern Inner Mongolia, NE China: Implications for igneous petrogenesis, tectonic setting, and geodynamic evolution of the south-eastern Central Asian Orogenic Belt. *Lithos* **2020**, *362–363*, 105480. [[CrossRef](#)]
35. Chew, D.M.; Petrus, J.A.; Kamber, B.S. U–Pb LA-ICP-MS dating using accessory mineral standards with variable common Pb. *Chem. Geol.* **2014**, *363*, 185–199. [[CrossRef](#)]
36. Chew, D.M.; Sylvester, P.J.; Tubrett, M.N. U–Pb and Th–Pb dating of apatite by LA-ICP-MS. *Chem. Geol.* **2011**, *280*, 200–216. [[CrossRef](#)]
37. Black, L.P.; Kamo, S.L.; Allen, C.M.; Aleinikoff, J.N.; Davis, D.W.; Korsch, R.J.; Foudoulis, C. TEMORA 1 a new zircon standard for Phanerozoic U–Pb geochronology. *Chem. Geol.* **2003**, *200*, 155–170. [[CrossRef](#)]
38. Luan, Y.; He, K.; Tan, X.J. In situ U–Pb dating and trace element determination of standard zircons by LA-ICP-MS. *Geol. Bull. China* **2019**, *38*, 1206–1218, (In Chinese with English Abstract).
39. Chiaradia, M.; Schaltegger, U.; Spikings, R.; Wotzlaw, J.F.; Ovtcharova, M. How accurately can we date the duration of magmatic hydrothermal events in porphyry systems?—An invited paper. *Econ. Geol.* **2013**, *108*, 565–584. [[CrossRef](#)]
40. Meinert, L.D.; Dipple, G.M.; Nicolescu, S. World skarn deposits. In *Economic Geology 100th Anniversary Volume*; Society of Economic Geologists, Inc.: Littleton, CO, USA, 2005; pp. 299–336.
41. Lima, S.M.; Corfu, F.; Neiva, A.M.R.; Ramos, J.M.F. U–Pb ID-TIMS dating applied to U-rich inclusions in garnet. *Amer. Miner.* **2012**, *97*, 800–806. [[CrossRef](#)]
42. Wafforn, S.; Seman, S.; Kyle, J.R.; Stockli, D.; Leys, C.; Sonbait, D.; Cloos, M. Andradite garnet U–Pb geochronology of the big Gossan skarn, Ertsberg–Grasberg mining district, Indonesia. *Econ. Geol.* **2018**, *113*, 769–778. [[CrossRef](#)]
43. Alexander, E.M.; Alexei, V.I.; Vadim, S.K.; Adam, A.; Tamara, Y.Y.; Timur, V.D. Contact metamorphic and metasomatic processes at the Kharaelakh Intrusion, Oktyabrsk Deposit, Norilsk–Talnakh ore district: Application of LA-ICP-MS dating of perovskite, apatite, garnet, and titanite. *Econ. Geol.* **2020**, *115*, 1213–1226.
44. Li, Y.X.; Kang, Z.Q.; Xu, J.F.; Yang, F.; Liu, D.M.; Shan, C.X. Chronological, Geochemical Characteristics and Geological Significance of Volcanic Rocks in the Late Early Cretaceous in Southeast Guangxi. *Earth Sci.* **2021**, 1–28, (In Chinese with English Abstract). [[CrossRef](#)]
45. Liu, Y.; Fang, N.; Qiang, M.; Jia, L.; Song, C. The Cretaceous igneous rocks in southeastern Guangxi and their implication for tectonic environment in southwestern South China Block. *Open. Geosci.* **2020**, *12*, 518–531. [[CrossRef](#)]
46. Wang, X.Y. Late Yanshanian Magmatism and W-Mineralization in Yunkai Region, Guangxi Province. Ph.D. Thesis, China University of Geosciences, Wuhan, China, 2017.
47. Li, J.; Zhang, Y.; Dong, S.; Johnston, S.T. Cretaceous tectonic evolution of South China: A preliminary synthesis. *Earth Sci. Rev.* **2014**, *134*, 98–136. [[CrossRef](#)]
48. Yang, J.B.; Zhao, Z.D.; Hou, Q.Y.; Niu, Y.L.; Mo, X.X.; Sheng, D.; Wang, L.L. Petrogenesis of Cretaceous (133–84 Ma) intermediate dykes and host granites in southeastern China: Implications for lithospheric extension, continental crustal growth, and geodynamics of Palaeo-Pacific subduction. *Lithos* **2018**, *296–299*, 195–211. [[CrossRef](#)]
49. Liu, L.; Xu, X.S.; Xia, Y. Cretaceous Pacific plate movement beneath SE China: Evidence from episodic volcanism and related intrusions. *Tectonophysics* **2014**, *614*, 170–184. [[CrossRef](#)]
50. Liu, L.; Xu, X.S.; Xia, Y. Asynchronizing paleo-Pacific slab rollback beneath SE China: Insights from the episodic Late Mesozoic volcanism. *Gondwana Res.* **2016**, *37*, 397–407. [[CrossRef](#)]
51. Zhang, L.P.; Hu, Y.B.; Liang, J.L.; Ireland, T.; Chen, Y.L.; Zhang, R.Q.; Sun, S.J.; Sun, W.D. Adakitic rocks associated with the shilu copper–molybdenum deposit in the Yangchun Basin, South China, and their tectonic implications. *Acta Geochim.* **2017**, *36*, 132–150. [[CrossRef](#)]
52. Liu, H.; Liao, R.; Zhang, L.; Li, C.; Sun, W. Plate subduction, oxygen fugacity, and mineralization. *J. Oceanol. Limnol.* **2020**, *38*, 64–74. [[CrossRef](#)]
53. Li, J.H.; Cawood, P.A.; Ratschbacher, L.; Zhang, Y.Q.; Dong, S.W.; Xin, Y.J.; Yang, H.; Zhang, P.X. Building Southeast China in the late Mesozoic: Insights from alternating episodes of shortening and extension along the Lianhuashan fault zone. *Earth Sci. Rev.* **2020**, *201*, 103056. [[CrossRef](#)]

54. Suo, Y.H.; Li, S.Z.; Jin, C.; Zhang, Y.; Zhou, J.; Li, X.Y.; Wang, P.C.; Liu, Z.; Somerville, L. Eastward tectonic migration and transition of the Jurassic–Cretaceous Andean-type continental margin along Southeast China. *Earth Sci. Rev.* **2019**, *196*, 102884. [[CrossRef](#)]
55. Li, S.Z.; Suo, Y.H.; Li, X.Y.; Zhou, J.; Santosh, M.; Wang, P.C.; Wang, G.Z.; Guo, L.L.; Yu, S.Y.; Lan, H.Y.; et al. Mesozoic tectono-magmatic response in the East Asian ocean-continent connection zone to subduction of the Paleo-Pacific Plate. *Earth Sci. Rev.* **2019**, *192*, 91–137. [[CrossRef](#)]
56. Li, J.H.; Ma, Z.L.; Zhang, Y.Q.; Dong, S.W.; Li, Y.; Lu, M.A.; Tan, J.Q. Tectonic evolution of Cretaceous extensional basins in Zhejiang Province, eastern South China: Structural and geochronological constraints. *Int. Geol. Rev.* **2014**, *56*, 1602–1629. [[CrossRef](#)]
57. Zhou, X.M.; Sun, T.; Shen, W.Z.; Shu, L.S.; Niu, Y.L. Petrogenesis of Mesozoic granitoids and volcanic rocks in South China: A response to tectonic evolution. *Episodes* **2006**, *9*, 26–33. [[CrossRef](#)]
58. Chu, Y.; Lin, W.; Faure, M.; Xue, Z.H.; Ji, W.B.; Feng, Z.T. Cretaceous episodic extension in the South China Block, East Asia: Evidence from the Yuechengling Massif of central South China. *Tectonics* **2019**, *38*, 3675–3702. [[CrossRef](#)]
59. Shu, L.S.; Zhou, X.M.; Deng, P.; Wang, B.; Jiang, S.Y.; Yu, J.H.; Zhao, X.X. Mesozoic tectonic evolution of the Southeast China Block: New insights from basin analysis. *J. Asian Earth Sci.* **2009**, *34*, 376–391. [[CrossRef](#)]
60. Sun, W. Initiation and evolution of the South China Sea: An overview. *Acta Geochim.* **2016**, *35*, 215–225. [[CrossRef](#)]
61. Zhou, J.X.; Li, W.C. Evolution and metallogeny of the Sanjiang arc-back arc basin system in the Eastern Tethys: An introduction. *J. Asian Earth Sci.* **2021**, *222*, 104961. [[CrossRef](#)]
62. Yang, Q.J.; Li, C.C.; Yang, J.B. The geological and geochemical characteristics of volcanic rocks in Shuiwen Basin of Guangxi: Magmatic activity response to Mesozoic strike-slip process in Cenxi-Bobai Fault zone. *Miner. Resour. Geol.* **2022**, *36*, 781–795, (In Chinese with English Abstract).
63. Li, C. The Evolution and Geological Significance of Complex Rock Mass in Xintang City, Cenxi City, Guangxi. Master's Thesis, Guilin University of Technology, Guilin, China, 2018. (In Chinese with English Abstract).

Disclaimer/Publisher's Note: The statements, opinions and data contained in all publications are solely those of the individual author(s) and contributor(s) and not of MDPI and/or the editor(s). MDPI and/or the editor(s) disclaim responsibility for any injury to people or property resulting from any ideas, methods, instructions or products referred to in the content.